

1 **Merging ground-based sunshine duration**  
2 **observations with satellite cloud and aerosol**  
3 **retrievals to produce high resolution long-**  
4 **term surface solar radiation over China**

5 Fei Feng<sup>1</sup> † and Kaicun Wang<sup>2</sup> †

6 1. College of Forestry, Beijing Forestry University, Beijing 100083, China

7 2. State Key Laboratory of Earth Surface Processes and Resource Ecology, College of  
8 Global Change and Earth System Science, Beijing Normal University, Beijing, 100875,  
9 China

10 †These authors contributed equally to this work

11 **Corresponding Author:**

12 Fei Feng, College of Forestry, Beijing Forestry University, Email:  
13 [forgetbear@bjfu.edu.cn](mailto:forgetbear@bjfu.edu.cn);

14 Kaicun Wang, College of Global Change and Earth System Science, Beijing Normal  
15 University. Email: [kewang@bnu.edu.cn](mailto:kewang@bnu.edu.cn); Tel: +086 10-58803143; Fax: +086 10-  
16 58800059.

17

18

19

20

## Abstract

Although great progress has been made in estimating surface solar radiation ( $R_s$ ) from meteorological observations, satellite retrieval and reanalysis, getting best estimated long-term variations in  $R_s$  are sorely needed for climate studies. It has been shown that sunshine duration (SunDu)-derived  $R_s$  data can provide reliable long-term variability, but are available at sparsely distributed weather stations. Here, we merge SunDu-derived  $R_s$  with satellite-derived cloud fraction and aerosol optical depth (AOD) to generate high spatial resolution ( $0.1^\circ$ )  $R_s$  over China from 2000 to 2017. The geographically weighted regression (GWR) and ordinary least squares regression (OLS) merging methods are compared, and GWR is found to perform better. Based on the SunDu-derived  $R_s$  from 97 meteorological observation stations, which are co-located with those that direct  $R_s$  measurement sites, the GWR incorporated with satellite cloud fraction and AOD data produces monthly  $R_s$  with  $R^2 = 0.97$  and standard deviation =  $11.14 \text{ W/m}^2$ , while GWR driven by only cloud fraction produces similar results with  $R^2 = 0.97$  and standard deviation =  $11.41 \text{ w/m}^2$ . This similarity is because SunDu-derived  $R_s$  has included the impact of aerosols. This finding can help to build long-term  $R_s$  variations based on cloud data, such as Advanced Very High Resolution Radiometer (AVHRR) cloud retrievals, especially before 2000, when satellite AOD retrievals are not unavailable. The merged  $R_s$  product at a spatial resolution of  $0.1^\circ$  in this study can be downloaded at <https://doi.pangaea.de/10.1594/PANGAEA.921847> (Feng and Wang, 2020).

## 47           **Introduction**

48           A clear knowledge of variations in surface solar radiation ( $R_s$ ) is vitally important  
49 for an improved understanding of the global climate system and its interaction with  
50 human activity (Jia et al., 2013; Myers, 2005; Schwarz et al., 2020; Wang and Dickinson,  
51 2013; Wild, 2009, 2017; Zell et al., 2015). Direct measurements have shown that  $R_s$  has  
52 significant decadal variability, namely, a decrease (global dimming) from the 1950s to  
53 the late 1980s and subsequent increase (global brightening) (Wild, 2009). The variation  
54 in  $R_s$  is closely related to the Earth's water cycle, the whole biosphere, and the amount  
55 of available solar energy. This situation emphasizes the urgency to develop reliable  $R_s$   
56 products to obtain the variability in  $R_s$ .

57           Great progress has been made in the detection of variability in  $R_s$  by  
58 meteorological observations, satellite retrieval and radiation transfer model simulations  
59 or reanalysis  $R_s$  products in previous studies (Rahman and Zhang, 2019; Wang et al.,  
60 2015). However, each estimation has its advantages and disadvantages. Direct observed  
61 data provide accurate  $R_s$  records at short time scales; however, careful calibration and  
62 instrument maintenance are needed to maintain its long-term homogeneity. Previous  
63 studies have reported that direct observed  $R_s$  over China may have major inhomogeneity  
64 problems due to sensitivity drift and instrument replacement (Wang, 2014; Wang et al.,  
65 2015; Yang et al., 2018). Before 1990, the imitations of the USSR pyranometers had  
66 different degradation rates of the thermopile, resulting in an important sensitivity drift.  
67 To overcome radiometer ageing problem, China replaced its instruments from 1990 to  
68 1993. However, the new solar trackers failed frequently and introduced a high data  
69 missing rate for the direct radiation component of  $R_s$  (Lu and Bian, 2012; Mo et al.,  
70 2008). After 1993, although the instruments were substantially improved, the Chinese-  
71 developed pyranometers still had high thermal offset with directional response errors,

72 and the stability of these instruments was also worse than that of the World  
73 Meteorological Organization (WMO) recommended first-class pyranometers (Lu et al.,  
74 2002; Lu and Bian, 2012; Yang et al., 2010). Yang et al. (2018) show that nearly half of  
75 observed  $R_s$  (60 out of the 119  $R_s$  observed stations) have inhomogeneity issues. These  
76 artificial changes points in observed  $R_s$  are mainly caused by instrument change (42  
77 shifts), stations relocation (34 shifts), observation schedule change (20 shifts) and  
78 remaining 64 changepoints could not be identified.

79 SunDu data are relatively widely distributed and have a long-term record  
80 (Sanchezlorenzo et al., 2009; Wild, 2009). Existing studies have also confirmed that  
81 SunDu-derived  $R_s$  data are reliable  $R_s$  data, which can capture long-term trends of  $R_s$   
82 and reflect the impacts of both aerosols and clouds at time scales ranging from daily to  
83 decadal (Feng and Wang, 2019; Manara et al., 2015; Sanchezlorenzo et al., 2013;  
84 Sanchezromero et al., 2014; Tang et al., 2011; Wang et al., 2012b; Wild, 2016). Even  
85 though, SunDu data do not provide a direct estimate of  $R_s$  and have the different  
86 sensitivity of atmospheric turbidity changes, compared with  $R_s$  observations, they are  
87 still a good proxy for variations of  $R_s$  (Manara et al., 2017).

88 Sunshine duration observations collected at weather stations in China have been  
89 used to reconstruct long-term  $R_s$  (Che et al., 2005; Feng et al., 2019; He et al., 2018; He  
90 and Wang, 2020; Jin et al., 2005; Shi et al., 2008; Yang et al., 2006; Yang et al., 2020).  
91 Based on the global SunDu-derived  $R_s$  records, He et al. (2018) found that SunDu  
92 permitted a revisit of global dimming from the 1950s to the 1980s over China, Europe,  
93 and the USA, with brightening from 1980 to 2009 in Europe and a declining trend  $R_s$   
94 from 1994 to 2010 in China. (Wang et al., 2015) found that the dimming trend from  
95 1961 to 1990 and nearly constant zero trend after 1990 over China, as calculated from  
96 the SunDu-derived  $R_s$ , was consistent with independent estimates of AOD (Luo et al.,

97 2001); they also observed changes in the diurnal temperature range (Wang et al., 2012a;  
98 Wang and Dickinson, 2013) and the observed pan evaporation (Yang et al., 2015).  
99 Although direct observations and SunDu-derived  $R_s$  can provide accurate long-term  
100 variations in  $R_s$ , both direct observations and sunshine duration records are often  
101 sparsely spatially distributed.

102 Satellite  $R_s$  retrievals and radiation transfer model simulations or reanalysis  $R_s$   
103 products can provide  $R_s$  estimation with global coverage at high spatial resolution.  
104 However, model simulations and reanalysis  $R_s$  products have substantial biases due to  
105 the deficiency of simulating cloud and aerosol quantities (Feng and Wang, 2019; Zhao  
106 et al., 2013). Previous comparative studies have shown that the accuracies of  $R_s$  from  
107 reanalyses are lower than those of satellite products (Wang et al., 2015; Zhang et al.,  
108 2016) due to the good capability of capturing the spatial distribution and dynamic  
109 evolution of clouds in satellite remote sensing data.

110 **Table 1** lists the current satellite-based  $R_s$  products, which have been widely  
111 validated in previous studies. Zhang et al. (2004) found that the monthly International  
112 Satellite Cloud Climatology Project-Flux Data (ISCCP-FD)  $R_s$  product had a positive  
113 bias of  $8.8 \text{ w/m}^2$  using Global Energy Balance Archive (GEBA) archived data as a  
114 reference. By comparing 1151 global sites, Zhang et al. (2015) evaluated four satellite-  
115 based  $R_s$  products, including ISCCP-FD, the Global Energy and Water Cycle  
116 Experiment-Surface Radiation Budget (GEWEX-SRB), the University of  
117 Maryland/Shortwave Radiation Budget (UMD-SRB) and the Earth's Radiant Energy  
118 System energy balanced and filled product (CERES EBAF), and concluded that CERES  
119 EBAF shows better agreement with observations than other products. A similar overall  
120 good performance of CERES EBAF can also be found (Feng and Wang, 2018; Ma et  
121 al., 2015).

122 **Table 1.** Current satellite-derived surface solar radiation ( $R_s$ ) products

Satellite $R_s$ product	Source	Spatial resolution	Time range
ISCCP-FD	ISCCP	2.5°	1983-2009
GEWEX-SRB	ISCCP-DX	1°	1983-2007
UMD-SRB	METEOSAT-5	0.5°	1983-2007
GLASS-DSR	Terra/Aqua, GOES, MSG, MTSAT	0.05°	2008-2010
CLARA-A2	AVHRR	0.25°	1982-2015
MCD18A1	Terra/Aqua, MODIS	5.6 km	2001-present
Himawari-8 SWSR	Himawari-8	5 km	2015-present
SSR-tang	ISCCP-HXG, ERA5, MODIS	10 km	1982-2017
Cloud_cci AVHRR-PMv3	AVHRR/CC4CL	0.05°	1982-2016

123

124 Although CERES EBAF uses more accurate input data to provide  $R_s$  data, its  
 125 spatial resolution is only 1° (Kato et al., 2018). Since 2010, new-generation  
 126 geostationary satellites have provided opportunities for high temporal and spatial  
 127 resolution  $R_s$  data, such as Himawari-8 (Hongrong et al., 2018; Letu et al., 2020).  
 128 However, the time span of the new-generation satellite-based  $R_s$  product is short. The  
 129 long-term AVHRR records provide the possibility of building long-term radiation  
 130 datasets. The CLOUD, Albedo and RADIATION dataset, the AVHRR-based data-second  
 131 edition (CLARA-A2), covers a long time period, but the spatial resolution is only 0.25°  
 132 (Karlsson et al., 2017). Recently, Tang et al. (2019) built a satellite-based  $R_s$  (SSR-tang)  
 133 dataset using ISCCP-HXG cloud data. By using a variety of cloud properties derived  
 134 from AVHRR, Stengel et al. (2020) presented the Cloud\_cci AVHRR-PMv3 dataset  
 135 generated within the Cloud\_cci project.

136 Validation against the BSRN data indicated that SSR-tang have the mean bias error  
 137 (MBE) of -11.5 W/m<sup>2</sup> and root mean square error (RMSE) of 113.5 W/m<sup>2</sup> for the  
 138 instantaneous  $R_s$  estimates at 10 km scale, but Tang et al. (2019) point out that care  
 139 should be taken when using this dataset for trend analysis due to the absent of realistic  
 140 aerosols input data. Stengel et al. (2020) also show that  $R_s$  derived from Cloud\_cci

141 AVHRR-PMv3 reveals a very good agreement against BSRN stations, with low  
142 standard deviations of  $13.8 \text{ W/m}^2$  and correlation coefficients above 0.98. While the  
143 bias for shortwave fluxes is small ( $1.9 \text{ W/m}^2$ ). However, default an aerosol optical depth  
144 of 0.05 or data from Aerosol cci Level-2 or NASA MODIS Level-2 aerosol data are  
145 used in BUGSrad model to calculate clear sky  $R_s$ , indicating that impact of aerosols is  
146 not perfect parameterized in Cloud\_cci AVHRR-PMv3.

147 On the other hand, the long-term cloud records also contain uncertainties. For  
148 example, ISCCP cloud products, which directly combine geostationary and polar  
149 orbiter satellite-based cloud data, have large inhomogeneity due to different amounts of  
150 data from polar orbit and geostationary satellites and their different capabilities for  
151 detecting low-level clouds (Dai et al., 2006; Evan et al., 2007). This inhomogeneity of  
152 the cloud products might introduce significant inhomogeneity to the  $R_s$  values  
153 calculated from the cloud products (Montero-Martín et al., 2020; Pfeifroth et al., 2018b),  
154 and  $R_s$  long-term variability estimation still needs improvement.

155 Efforts have been made to further improve  $R_s$  products. Merging multisource data  
156 has become an effective empirical method for improving the quality of  $R_s$  products  
157 (Camargo and Dorner, 2016; Feng and Wang, 2018; Hakuba et al., 2014; Journée et al.,  
158 2012; Lorenzo et al., 2017; Ruiz-Arias et al., 2015). For instance, to produce  
159 spatiotemporally consistent  $R_s$  data, multisource satellite data are used in Global LAnd  
160 Surface Satellite (GLASS)  $R_s$  products (Jin et al., 2013). By merging reanalysis and  
161 satellite  $R_s$  data by the probability density function-based method, the reanalysis  $R_s$   
162 biases can be substantially reduced (Feng and Wang, 2018). This finding suggests that  
163 fusion methods are effective ways to improve the estimation of  $R_s$ , especially when  $R_s$   
164 impact factors are considered (Feng and Wang, 2019). Although linear regression fusion  
165 methods can produce  $R_s$  data incorporated with  $R_s$  impact factors, the stable regression

166 parameters might have negative effects on the final fusion results due to the complex  
167 characteristics of  $R_s$  spatial-temporal variability.

168 On the other hand, the spatial resolution of  $R_s$  data is crucial for regional  
169 meteorology studies, as the minimum requirement of the spatial resolution of  $R_s$  data,  
170 as suggested by the Observing Systems Capabilities Analysis and Review of WMO  
171 OSCAR), is 20 km (Huang et al., 2019). Interpolation methods are often included in  $R_s$   
172 fusion methods to further improve the spatial resolutions of  $R_s$  data (Loghmari et al.,  
173 2018). For example, Zou et al. (2016) estimated global solar radiation using an artificial  
174 neural network based on an interpolation technique in southeast China. By integrating  
175  $R_s$  data from 13 ground stations with Meteosat Second Generation satellite  $R_s$  products,  
176 Journée and Bertrand (2010) found that kriging with the external drift interpolation  
177 method performed better than mean bias correction, interpolated bias correction and  
178 ordinary kriging with satellite-based correction. However, interpolation results have  
179 uncertainties due to the lack of detailed high spatial resolution information. Although  
180 traditional linear regression fusion methods can incorporate high spatial resolution data  
181 during the fusion process, the impacts of the stable regression parameters need further  
182 investigation.

183 The performances of different machine learning methods have been evaluated in  
184 many previous studies, including simulation  $R_s$  at regional scale with support of satellite  
185 retrievals (Wei et al., 2019; Yeom et al., 2019) and site scale by using routine  
186 meteorological observations (Cornejo-Bueno et al., 2019; Hou et al., 2020). Whatever  
187 models or training data are selected, the impacts of spatial relationship are not taken  
188 into account in these machine learning based model and therefore large number of input  
189 data are required to ensure accuracy.

190 Geographically weighted regression (GWR) is an extension of the traditional



191 regression model by allowing the relationships between dependent and explanatory  
192 variables to vary spatially. Researchers have examined and compared the applicability  
193 of GWR for the analysis of spatial data relative to that of other regression methods (Ali  
194 et al., 2007; Gao et al., 2006; Georganos et al., 2017; LeSage, 2004; Sheehan et al.,  
195 2012; Zhou et al., 2019a). Due to the large spatial heterogeneity of  $R_s$  over China, the  
196 GWR method might produce accurate  $R_s$  variability estimations with an improved  
197 spatial resolution.

198 This study is established to merge SunDu-derived  $R_s$  data with satellite-derived  
199 cloud fraction (CF) and AOD data to generate high spatial resolution ( $0.1^\circ$ )  $R_s$  over  
200 China from 2000 to 2017. The GWR and ordinary least squares (OLS) regression  
201 merging methods are compared. CF and AOD are important  $R_s$  impact factors, however,  
202 many long-term  $R_s$  satellite products use climatology aerosols data as input. Whether  
203 much improvement is made in merging SunDu-derived  $R_s$  by incorporating AOD is also  
204 evaluated in this study, instead of evaluating direct merging current  $R_s$  products with  
205 SunDu-derived  $R_s$ . Since current  $R_s$  high quality  $R_s$  such as CERES EBAF have low  
206 spatial resolution, the output of this study provides a reliable high resolution grid  $R_s$   
207 data to avoid the disadvantage of CERES EBAF for capturing the variability of  $R_s$   
208 within a 1 degree box and provide guidance to merge multisource data to generate long-  
209 term  $R_s$  data over China.

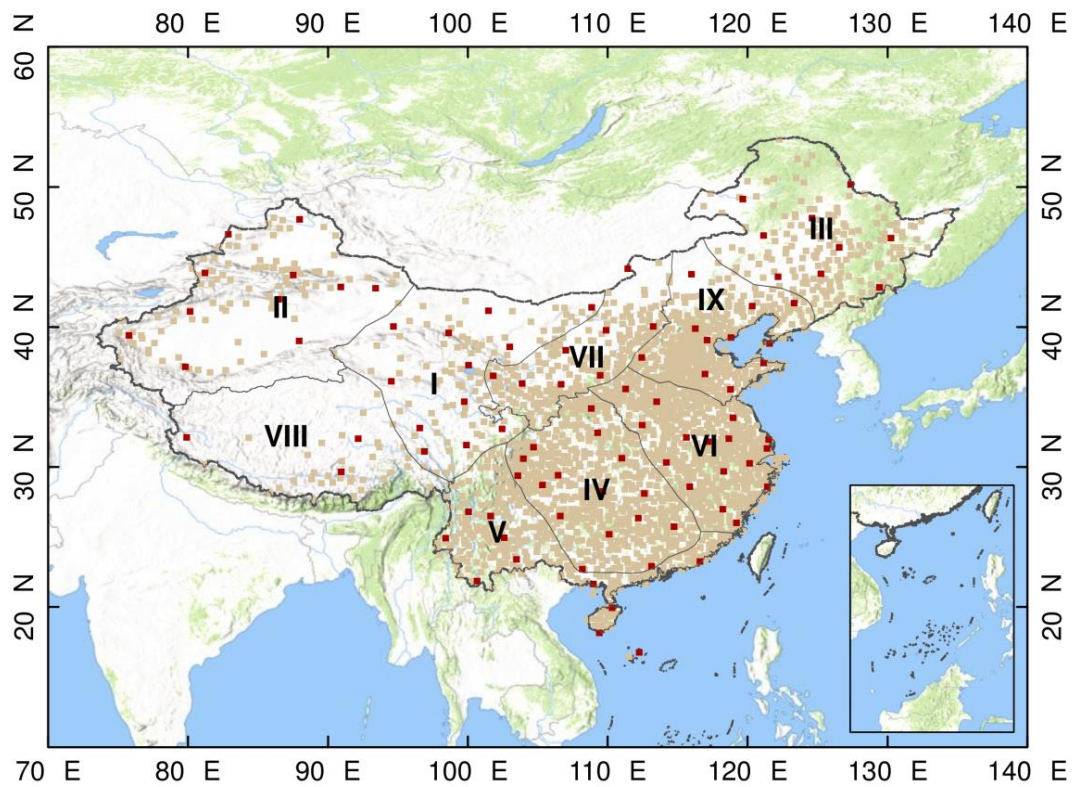
## 210 **1. Data and Methodology**

### 211 ***2.1. Ground-based observations***

#### 212 ***2.2.1 Direct observations***

213  $R_s$  direct observations from 2000 to 2017 are obtained from the China  
214 Meteorological Data Service Center (CMDC, <http://data/cma/cn/>) of the China  
215 Meteorological Administration (CMA). TBQ-2 pyranometers and DFY4 pyranometers

216 have been used to measure  $R_s$  since 1993. Daily  $R_s$  values from 97  $R_s$  stations are  
 217 collected, and we calculated monthly  $R_s$  values by averaging daily  $R_s$  values when daily  
 218 observed data are available for more than 15 days for each month at each radiation  
 219 station. These monthly  $R_s$  values from direct measurements and collocated SunDu-  
 220 derived  $R_s$  are used as independent reference data to investigate the performances of the  
 221 fusion methods (**Fig. 1**). The whole area over China is further divided into nine zones  
 222 by the K-mean cluster method based on geographic locations and multiyear mean  $R_s$   
 223 using 97  $R_s$  direct observation sites, as shown in **Figure 1**. The download instructions  
 224 of the  $R_s$  direct observations can be found in **table 2**.



225  
 226 **Figure 1.** The 2,400 sunshine duration (SunDu) merging sites are shown as light brown  
 227 points, and 97 independent validation sites, including  $R_s$  direct measurements and  
 228 SunDu-derived  $R_s$  measurements, are shown as brown red points. The whole region is  
 229 classified into nine subregions (I to IX) by the K-mean cluster method based on  
 230 geographic locations and multiyear mean  $R_s$  using 97  $R_s$  direct observation sites. The

231 base hillshade map was produced by an elevation map of China using the global digital  
 232 elevation model (DEM) derived from the Shuttle Radar Topography Mission 30  
 233 (SRTM30) dataset.

234

235

236 **Table 2.** Summary of availability information for all source data used in this study.

237 CMDC is the China Meteorological Data Service Center. SunDu is the sunshine

238 duration data.  $R_s$  is surface solar radiation and AOD is the aerosols optical depth.

Data Source	Derived Parameters	Spatial resolution	Version	Access Point	Notes	Reference
Direct $R_s$ measurement data from CMDC	$R_s$	-	Version 1.0	<a href="http://data/cma/cn/">http://data/cma/cn/</a>	Authentication is required for the China data use policy	-
SunDu observations and other meteorological data	$R_s$	-	Version 1.0	<a href="http://data/cma/cn/">http://data/cma/cn/</a>	Authentication is required for the China data use policy	-
CERES EBAF	$R_s$	1 degree	Ed4.1	<a href="https://ceres.larc.nasa.gov/data/#ebaf-level-3b">https://ceres.larc.nasa.gov/data/#ebaf-level-3b</a>	A email address to order the data	(Kato et al., 2018)
CERES SYN1deg	AOD	1 degree	Ed4A	<a href="https://ceres.larc.nasa.gov/data/#syn1deg-level-3">https://ceres.larc.nasa.gov/data/#syn1deg-level-3</a>	A email address to order the data	(Rutan et al., 2015)
MODAL2 M CLD	cloud fraction	0.1 degree	-	<a href="https://neo.sci.gsfc.nasa.gov/view.php?datasetId=MODAL2_M_CLD_FR">https://neo.sci.gsfc.nasa.gov/view.php?datasetId=MODAL2_M_CLD_FR</a>	Directly download	(Platnick et al., 2017)

239 **2.2.2 SunDu-derived  $R_s$**

240 Sunshine duration observations (SunDu) and other meteorological data (e.g., air

241 temperature, relative humidity and surface pressure) from 1980 to 2017, which were

242 collected from approximately 2,400 meteorological stations (<http://data/cma/cn/>) from  
 243 the CMA, are used to calculate the SunDu-derived  $R_s$  (**Fig. 1**).  $R_s$  values are calculated  
 244 following the method of the revised Ångström-Prescott equation (Eq. (1-2)) (He et al.,  
 245 2018; Wang, 2014; Wang et al., 2015; Yang et al., 2006).

$$246 \quad \frac{R_s}{R_c} = a_0 + a_1 \frac{n}{K} + a_2 \left(\frac{n}{K}\right)^2 \quad (1)$$

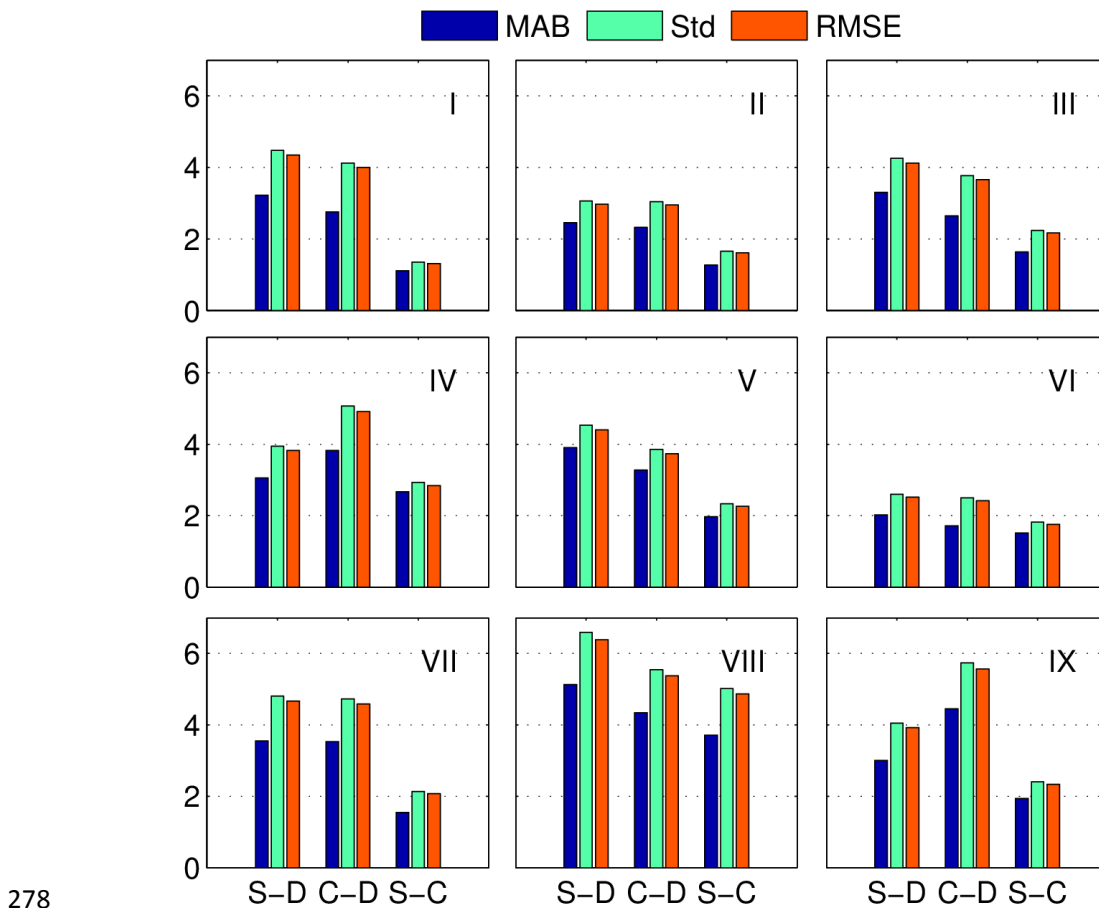
$$247 \quad R_c = \int (\tau_{c\_dir} + \tau_{c\_dif}) \times I_0 dt \quad (2)$$

248 where  $n$  represents the measured SunDu, and  $K$  represents the theoretical value of the  
 249 SunDu.  $a_0$ ,  $a_1$ , and  $a_2$  are the station-dependent parameters by tuning this equation with  
 250 measurements of  $R_s$  and SunDu and then the method is applied regionally (Wang, 2014).  
 251 Instead using observations from weather stations in Japan (Yang et al., 2006),  
 252 observations in CMA are used (Wang, 2014).  $R_c$  is the daily total solar radiation at the  
 253 surface under clear-sky conditions (Eq. 2).  $\tau_{c\_dir}$  and  $\tau_{c\_dif}$  represent the direct radiation  
 254 transmittance and the diffuse radiation transmittance under clear-sky conditions.  $I_0$  is  
 255 the solar irradiance at the top of the atmosphere (TOA). For the clear sky  $R_s$ ,  $\tau_{c\_dir}$  and  
 256  $\tau_{c\_dif}$  are calculated using a modified a broadband radiative transfer model by  
 257 simplifying Leckner's spectral model (Leckner, 1978), which the effect of transmittance  
 258 functions of permanent gas absorption, Rayleigh scattering, water vapour absorption,  
 259 ozone absorption, and aerosol extinction are parameterized using the surface air  
 260 temperature, surface pressure, precipitable water, the thickness of the ozone layer,  
 261 turbidity, sunshine duration as inputs (Yang et al., 2006). Calculation of  $R_s$  also includes  
 262 impacts of aerosols because SunDu is impacted by changes in both clouds and aerosols  
 263 (Wang, 2014).

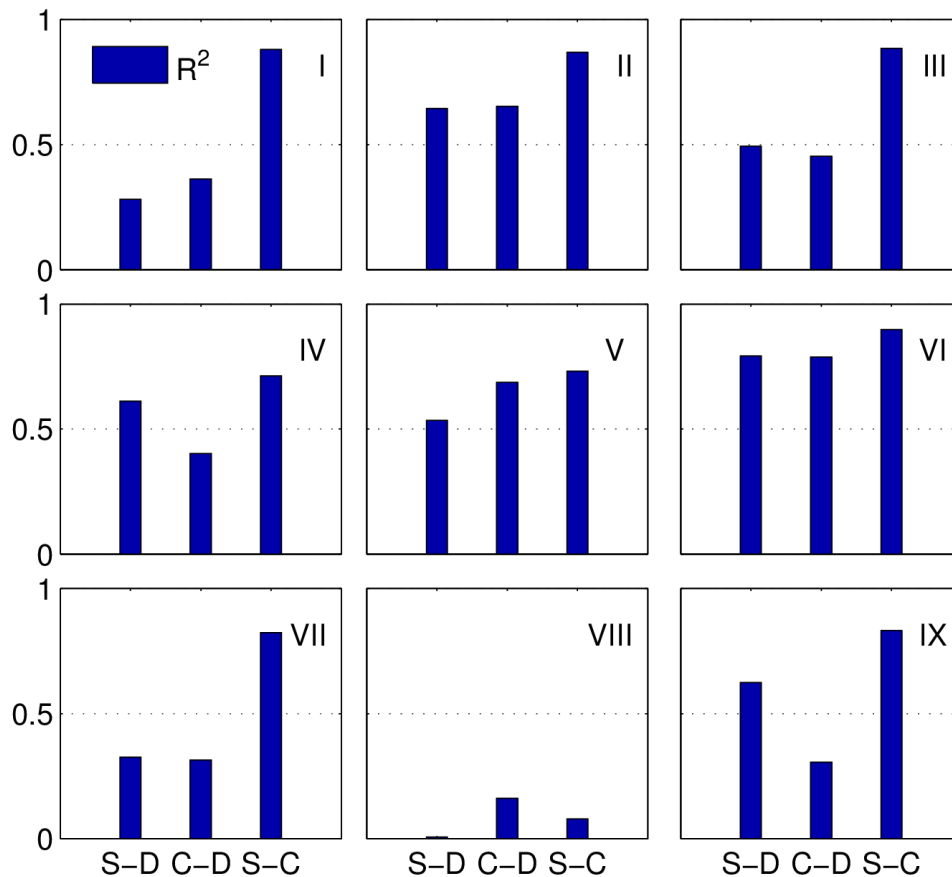
264 Based on the classified subregions using 97 direct  $R_s$  observations in **Figure 1**, the  
 265 intercomparison results in **Figure 2** and **Figure 3** show that the agreement between  
 266 SunDu-derived  $R_s$  and CERES EBAF  $R_s$  estimates is better than that between the direct

267 observations and SunDu-derived  $R_s$  estimates, which is likely due to the inhomogeneity  
 268 issue of direct  $R_s$  observations over China, as mentioned in many previous studies  
 269 (Wang, 2014; Yang et al., 2018). The satellite  $R_s$  retrievals and SunDu derived  $R_s$  are  
 270 totally independent, but the high agreements of these two datasets indicate that they  
 271 both are of higher accuracy. Similar results are also reported by (Wang et al., 2015) that  
 272 low agreement between SunDu derived  $R_s$  and direct  $R_s$  observation is likely due to the  
 273 directional response errors of the direct observations of  $R_s$ .

274 The SunDu-derived  $R_s$  observations, excluding SunDu observations located at  
 275 direct observation sites, are used for merging. Ten percent merging observations are  
 276 randomly selected for GWR parameter optimization. The download instructions of the  
 277 SunDu observations can be found in **table 2**.



279 **Figure 2.** Statistical summary of annual anomaly  $R_s$  from direct observed  $R_s$ , SunDu-  
 280 derived  $R_s$  and CERES EBAF  $R_s$  estimates in different subregions. The statistics include  
 281 the mean absolute bias (MAB), standard deviation (Std) and root mean square error  
 282 (RMSE). We use MAB due to the cancelling out effect of positive bias and negative  
 283 bias. Nine subregions (I to IX) over China are shown in Figure 1. S-D represent  
 284 comparisons between SunDu-derived  $R_s$  and directly observed  $R_s$ . C-D represent  
 285 comparison between CERES EBAF  $R_s$  and directly observed  $R_s$ . S-C represent  
 286 comparisons between SunDu-derived  $R_s$  and CERES EBAF  $R_s$ . The unit of y-axis are  
 287  $w/m^2$ .



288  
 289 **Figure 3.** Similar to Figure 2, but this statistical summary is for  $R^2$ .

290

291 **2.2. Satellite data**

292  $R_s$  data from the Clouds and Earth's Radiant Energy System energy balanced and

293 filled product (CERES Synoptic (CERES) EBAF) surface product (edition 4.1) (Kato  
294 et al., 2018), cloud fraction from MODAL2 M CLD data product (Platnick et al., 2017)  
295 and AOD from the CERES SYN1deg) edition 4A product (Doelling et al., 2013) are  
296 collected in this study. CERES EBAF  $R_s$  data are used as reference data. AOD from  
297 CERES SYN1deg and cloud fraction from MODAL2 M CLD are used as input data for  
298 fusion methods.

299 CERES is a 3-channel radiometer measuring three filtered radiances, including  
300 shortwave (0.3-5  $\mu\text{m}$ ), total (0.3-200  $\mu\text{m}$ ) and window (8-12  $\mu\text{m}$ ).  $R_s$  from CERES  
301 EBAF are adjusted using radiative kernels, including bias correction and Lagrange  
302 multiplier processes. The input data of CERES EBAF are adjusted during the product  
303 generating process constrained by CERES observations at the TOA. The biases in  
304 temperature and specific humidity from the Goddard Earth Observing System (GEOS)  
305 reanalysis are adjusted by atmospheric infrared sounder (AIRS) data. Cloud properties,  
306 such as optical thickness and emissivity, from MODIS and geostationary satellites are  
307 constrained by cloud profiling radar, Cloud-Aerosol Lidar, and Infrared Pathfinder  
308 Satellite Observations (CALIPSO) detectors and CloudSat. The uncertainties of  
309 CERES EBAF data, reported by (Kato et al., 2018), in all sky global annual mean  $R_s$  is  
310  $4 \text{ W m}^{-2}$ . Previous studies (Feng and Wang, 2019; Feng and Wang, 2018; Ma et al.,  
311 2015; Wang et al., 2015) have shown that the CERES EBAF surface product provides  
312 reliable estimations of  $R_s$ .

313 CERES SYN1deg AOD derived from an aerosol transport model, named  
314 Atmospheric Transport and Chemistry Modelling (MATCH) (Collins et al., 2001),  
315 which assimilates MODIS AOD data, is used to obtain spatiotemporally consistent  
316 AOD data. Different aerosol constituents, including small dust ( $<0.5 \mu\text{m}$ ), large dust  
317 ( $>0.5 \mu\text{m}$ ), stratosphere, sea salt, soot and soluble, are used to compute the optical

318 thickness for a given constituent optical thickness for a given constituent. We did not  
319 use AOD from MODIS, because MODIS AOD conation missing values and can't meet  
320 the requirements of spatiotemporal continuity of AOD input in this study. In addition,  
321 MODIS AOD is only available under clear sky conditions while AOD provided by the  
322 assimilation system is averaged under all conditions.

323 Cloud fraction data from MODAL2 M CLD are collected as input cloud fraction  
324 data with a spatial resolution of  $0.1^\circ$  and time span from 2000 to 2017 (Platnick et al.,  
325 2017). The MODAL2 M CLD data are synthesized based on the cloud data from  
326 MOD06. Cloud fraction data from MOD06 are generated by the cloud mask product of  
327 MOD35 with a spatial resolution of 1 km. The MOD35 cloud mask is determined by  
328 applying appropriate single field of view (FOV) spectral tests to each pixel with a series  
329 of visible and infrared threshold and consistency tests. Each land type has different  
330 algorithms and thresholds for the tests. For each pixel test, an individual confidence  
331 flag is determined and then combined to produce the final cloud mask flag. The three  
332 confidence levels included in the cloud mask flag output are (i) high confidence for  
333 cloudless pixels (Group confidence values  $> 0.95$ ); (ii) low confidence for unobstructed  
334 views on the surface (Group confidence values  $Q \leq 0.66$ ); and (iii) values between 0.66  
335 and 0.95, and spatial and temporal continuity tests are further applied to determine  
336 whether the pixel is absolutely cloudless. Then, the cloud fraction is calculated from  
337 the 5 x 5-km cloud mask pixel groupings, i.e., given the 25 pixels in the group, the  
338 cloud fraction for the group equals the number of cloudy pixels divided by 25.

### 339 **2.3. Methods**

#### 340 **2.3.1 Fusion models**

341 OLS regression and GWR are used to build fusion methods for estimating  $R_s$  data.  
342 Clouds fraction and AOD have been important factors that affect variations in  $R_s$ . We  
343 compare different combinations of input data for the fusion methods, which can be



344 classified into two types. The first type only contains cloud fraction data. The second  
 345 type contains clouds fraction and AOD (Feng and Wang, 2020).

346 The OLS regression model is a commonly used model to estimate dependent  
 347 variables by to minimizing the sum of square differences between the independent and  
 348 dependent variables. GWR is a regression model that allows the relationships between  
 349 the independent and dependent variables to vary by locality (Brunsdon et al., 2010;  
 350 Brunsdon et al., 1998). GWR deviates from the assumption of homoskedasticity or  
 351 static variance but calculates a specific variance for data within a zone or search radius  
 352 of each predictor variable (Brunsdon et al., 1998; Fotheringham et al., 1996; Sheehan  
 353 et al., 2012). The regression coefficients in GWR are not based on global information;  
 354 rather, they vary with location, which is generated by a local regression estimation using  
 355 subsampled data from the nearest neighbouring observations. The principle of GWR is  
 356 described as follows:

$$y_i = \delta(i) + \sum_k \delta_k(i)x_{ik} + \varepsilon_i \quad (3)$$

357 where  $y_i$  is the value of  $R_s$  unit  $i$ ;  $i=1,2,\dots,n$ ,  $n$  denotes location  $i$ ,  $x_{ik}$  indicates the value  
 358 of the  $x_{ik}$  variable, such as cloud fraction and AOD, and  $\varepsilon$  denotes the residuals.  $\delta(i)$  is  
 359 the regression intercept.  $\delta_{k(i)}$  is the vector of regression coefficients determined by  
 360 spatial weighting function  $w_{(i)}$ , which is the weighting function quantifying the  
 361 proximities of location  $i$  to its neighbouring observation sites;  $X$  is the variable matrix,  
 362 and  $b$  is the bias vector.

$$\delta_k(i) = (X^T w(i)X)^{-1} X^T w(i)b \quad (4)$$

363 The weighting functions are generally determined using the threshold method,  
 364 inverse distance method, Gauss function method, and Bi-square method. Due to the  
 365 irregular distribution of observation sites and computer ability, the adaptive Gaussian

366 function method is selected as a weighting function that varies in extent as a function  
 367 of  $R_s$  observation site density.

$$w_{ij} = \exp(-(d_{ij}/b)^2) \quad (5)$$

368 where  $w_{ij}$  is the weighting function for observation site  $j$  that refers to location  $i$ ;  $d_{ij}$   
 369 denotes the Euclidian distance between  $j$  and  $i$ ; and  $b$  is the size of the neighbourhood,  
 370 the maximum distance away from regression location  $i$ , called “bandwidth”, which is  
 371 determined by the number of nearest neighbour points (NNPs).

### 372 2.3.2 GWR parameter comparison

373 To perform the local regression for every local area, the numbers of NNPs are  
 374 required to estimate spatially varying relationships between CF, AOD and  $R_s$  in the  
 375 GWR-based fused method. To identify the best combination of parameter values, we  
 376 test the numbers of NNPs ranging from 29 to 1000. Ten percent of merging SunDu-  
 377 derived  $R_s$  data are randomly selected to validate these GWR parameters (**Fig. 1**). The  
 378 results show that  $R^2$  increases and bias decreases when the number of NNPs decreases.  
 379 However, when the NNP is smaller than 30, the GWR-based fusion method produces  
 380 spatially incomplete  $R_s$  data due to the local collinearity problem with large spatial  
 381 variability. Therefore, 30 is selected as the NNP parameter (**Table 3**).

382

383 **Table 3.** Statistical summary of GWR parameter optimization. NPP is the number of  
 384 nearest neighbour points. GWR-CF presents the GWR-based fused method using only  
 385 cloud fraction (CF) input, and GWR-CF-AOD presents that of using both CF and  
 386 aerosol optical depth (AOD) as input. MAB is the mean absolute bias. Std is the  
 387 standard deviation. RMSE is the root mean square error.

NNP	GWR-CF					GWR-CF-AOD				
	$R^2$	Bias	MAB	Std	RMSE	$R^2$	Bias	MAB	Std	RMSE
29	0.91	-0.21	7.45	9.90	9.90	0.91	-0.13	7.47	9.93	9.92
30	0.91	-0.23	7.45	9.90	9.90	0.91	-0.14	7.47	9.92	9.91

31	0.91	-0.24	7.45	9.90	9.90	0.91	-0.14	7.47	9.91	9.91
32	0.91	-0.25	7.46	9.91	9.91	0.91	-0.14	7.47	9.91	9.90
33	0.91	-0.26	7.47	9.92	9.92	0.91	-0.15	7.46	9.90	9.90
34	0.91	-0.27	7.47	9.93	9.93	0.91	-0.14	7.46	9.90	9.89
35	0.91	-0.28	7.48	9.94	9.94	0.91	-0.14	7.46	9.89	9.88
36	0.91	-0.28	7.49	9.94	9.94	0.91	-0.14	7.46	9.89	9.88
37	0.91	-0.29	7.49	9.95	9.95	0.91	-0.14	7.46	9.88	9.87
38	0.91	-0.30	7.50	9.96	9.96	0.91	-0.14	7.46	9.88	9.87
39	0.91	-0.31	7.51	9.98	9.98	0.91	-0.14	7.46	9.87	9.87
40	0.91	-0.32	7.52	9.99	9.99	0.91	-0.14	7.46	9.87	9.87
50	0.90	-0.38	7.62	10.12	10.12	0.91	-0.12	7.51	9.91	9.91
100	0.89	-0.57	8.20	10.90	10.91	0.90	-0.02	7.86	10.31	10.30
500	0.81	-1.08	10.89	14.50	14.54	0.86	0.20	9.55	12.45	12.45
1000	0.75	-1.13	12.60	16.57	16.61	0.82	0.26	10.68	13.84	13.85

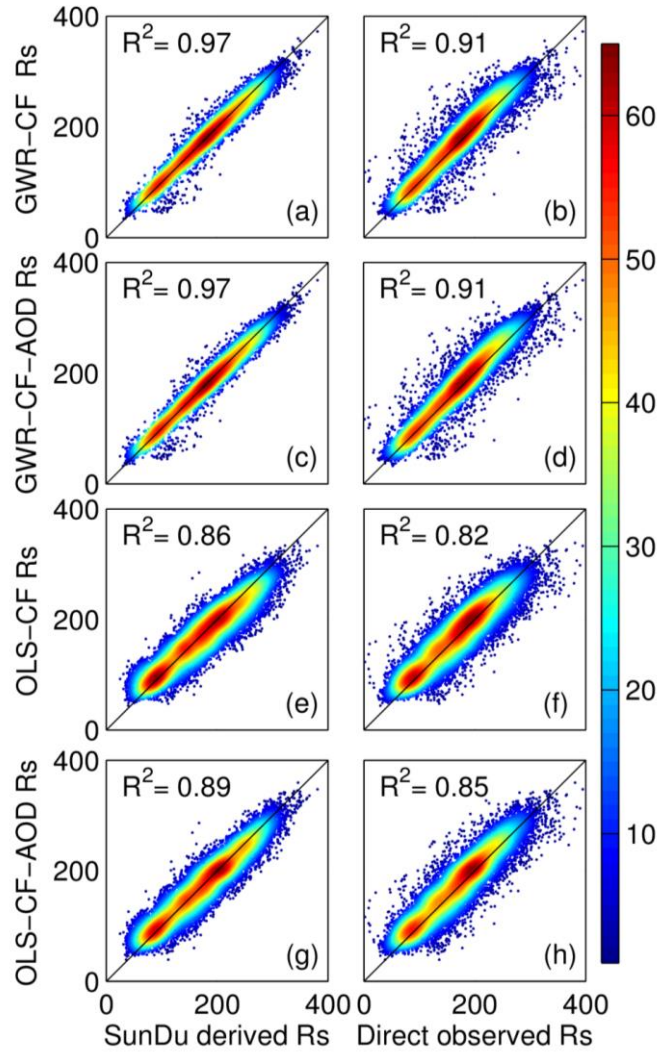
388

### 389 **3. Results**

#### 390 **3.1 Site validation**

391 Based on the independent SunDu validation sites, both the GWR and OLS  
392 methods explain 97%~86% of  $R_s$  variability (**Fig. 4**). The GWR method generally  
393 shows an improved performance compared with the OLS method due to the  
394 representativeness of the spatial heterogeneity relationship between  $R_s$  and its impact  
395 factors in GWR. Both the GWR and OLS methods produce better simulations of  $R_s$  if  
396 satellite and AOD data are incorporated.

397 Direct observations from 2000 to 2016 are also used to further evaluate the  
398 performance of the fusion methods (**Fig. 4**). The comparative result shows that both  
399 fusion methods show slightly reduced performances when using direct  $R_s$  observations  
400 rather than the SunDu-derived  $R_s$ . Both the GWR and OLS methods explain 91%~82%  
401 of  $R_s$  variability by using direct observations as reference data. Similarly, the GWR  
402 method exhibits better performances than the OLS-based fusion method, with an  $R^2$  of  
403 0.91 and root mean square error (RMSE) ranging from 19.89 to 19.97  $W/m^2$  at the  
404 monthly time scale (**Table 4**).



405

406 **Figure 4.** Comparison of surface solar radiation ( $R_s$ ) derived from the GWR method  
 407 and the OLS method. Subplots (a, c, e, g) represent validation results using SunDu-  
 408 derived  $R_s$  data as a reference, while that of subplots (b, d, f, h) use directly observed  
 409  $R_s$  data. Subplots (a, b, c, d) denote the GWR validation results, and subplots (e, f, g, h)  
 410 denote the OLS validation results.

411

412 **Table 4.** Validation of fusion methods driven by cloud fraction (CF) and AOD. GWR-  
 413 CF and OLS-CF represent the GWR fusion method and OLS fusion method driven only  
 414 by CF. GWR-CF-AOD and OLS-CF-AOD represent GWR and OLS fusion methods  
 415 driven by CF and AOD, respectively.

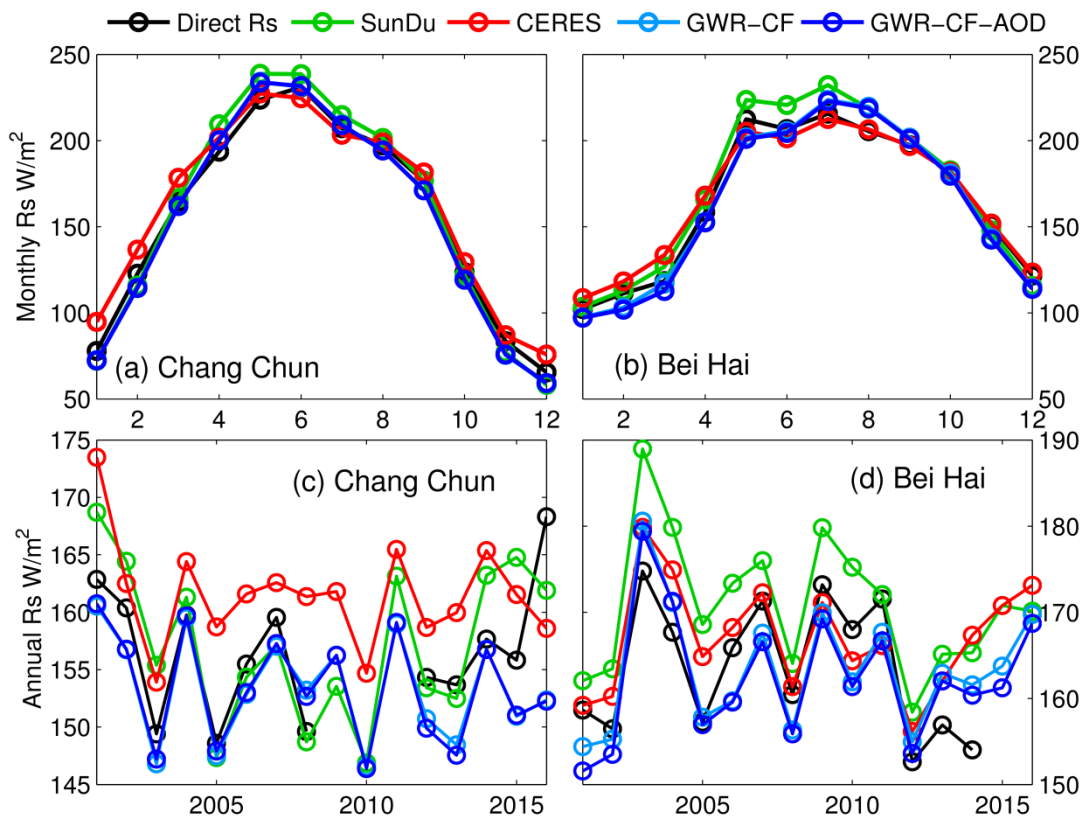
	Time scale	Ref	R2	Bias	Std	RMSE
GWR-CF	monthly	SunDu $R_s$	0.97	-1.17	11.41	11.47
GWR-CF-AOD	monthly	SunDu $R_s$	0.97	-0.82	11.14	11.17
OLS-CF	monthly	SunDu $R_s$	0.86	-3.80	25.03	25.32
OLS-CF-AOD	monthly	SunDu $R_s$	0.89	-1.37	22.10	22.15
GWR-CF	monthly	Direct Obs	0.91	4.88	19.29	19.89
GWR-CF-AOD	monthly	Direct Obs	0.91	5.24	19.27	19.97
OLS-CF	monthly	Direct Obs	0.82	2.18	26.73	26.82
OLS-CF-AOD	monthly	Direct Obs	0.85	4.64	24.71	25.15
GWR-CF	spring	SunDu $R_s$	0.95	-1.3	11.5	11.57
GWR-CF-AOD	spring	SunDu $R_s$	0.95	-0.86	11.2	11.23
OLS-CF	spring	SunDu $R_s$	0.77	-4.97	23.65	24.16
OLS-CF-AOD	spring	SunDu $R_s$	0.84	-1.35	19.85	19.9
GWR-CF	summer	SunDu $R_s$	0.9	-2.09	14.08	14.23
GWR-CF-AOD	summer	SunDu $R_s$	0.9	-1.38	13.76	13.82
OLS-CF	summer	SunDu $R_s$	0.65	-6.49	26.18	26.97
OLS-CF-AOD	summer	SunDu $R_s$	0.77	-1.37	21.17	21.22
GWR-CF	autumn	SunDu $R_s$	0.95	-1.27	9.48	9.56
GWR-CF-AOD	autumn	SunDu $R_s$	0.96	-1.04	9.17	9.23
OLS-CF	autumn	SunDu $R_s$	0.67	-3.22	25.62	25.82
OLS-CF-AOD	autumn	SunDu $R_s$	0.71	-1.97	23.79	23.87
GWR-CF	winter	SunDu $R_s$	0.94	0.01	9.87	9.86
GWR-CF-AOD	winter	SunDu $R_s$	0.94	0.04	9.78	9.78
OLS-CF	winter	SunDu $R_s$	0.63	-0.37	24.16	24.16
OLS-CF-AOD	winter	SunDu $R_s$	0.65	-0.78	23.41	23.42
GWR-CF	annual	Direct Obs	0.37	5.62	4.73	10.42
GWR-CF-AOD	annual	Direct Obs	0.37	5.98	4.79	10.53
OLS-CF	annual	Direct Obs	0.30	3.06	5.01	15.01
OLS-CF-AOD	annual	Direct Obs	0.33	5.45	4.89	13.34
GWR-CF	annual	SunDu $R_s$	0.57	-1.19	4.30	6.76
GWR-CF-AOD	annual	SunDu $R_s$	0.58	-0.84	4.30	6.68
OLS-CF	annual	SunDu $R_s$	0.35	-3.58	5.63	15.17
OLS-CF-AOD	annual	SunDu $R_s$	0.39	-1.23	5.44	13.40
GWR-CF	annual mean	SunDu $R_s$	0.94	-1.50	6.63	6.76
GWR-CF-AOD	annual mean	SunDu $R_s$	0.95	-1.15	6.41	6.47
OLS-CF	annual mean	SunDu $R_s$	0.62	-3.90	17.11	17.46
OLS-CF-AOD	annual mean	SunDu $R_s$	0.71	-1.58	14.90	14.90
GWR-CF	annual mean	Direct Obs	0.89	5.08	9.85	11.03
GWR-CF-AOD	annual mean	Direct Obs	0.89	5.43	9.75	11.11
OLS-CF	annual mean	Direct Obs	0.70	2.57	16.31	16.42
OLS-CF-AOD	annual mean	Direct Obs	0.77	4.88	14.00	14.75

416

### 417 3.2 Seasonal and annual variations in $R_s$

418 To analyse the impacts of AOD on the GWR fusion results, the GWR driven with  
419 only CF (GWR-CF) and GWR driven with CF and AOD (GWR-CF-AOD) are  
420 compared. Two validation sites (Chang Chun, 43.87°N 125.33°E and Bei Hai, 21.72°N

421 109.08°E) are randomly selected to evaluate the seasonal and annual variations in  $R_s$ ,  
 422 derived from the GWR method (**Fig. 5**). The multiyear mean of AOD from Changchun  
 423 and BeiHai are 0.49 and 0.70, respectively. As shown in **subplots (a and b)**, both GWR-  
 424 CF and GWR-CF-AOD produce similar seasonal variation patterns compared with  
 425 SunDu-derived  $R_s$  and CERES EBAF  $R_s$  data. Small differences are found in the  
 426 seasonal variation in  $R_s$  derived from GWR regardless of whether AOD was  
 427 incorporated. Examination of the annual variation  $R_s$  from the GWR-CF and GWR-CF-  
 428 AOD are shown in **subplots (c and d)** of **Figure 5**. The two fusion methods also  
 429 produce similar annual  $R_s$  variations. The similar performances of the GWR-CF and  
 430 GWR-CF-AOD might suggest that the impacts of AOD have already been included in  
 431 the SunDu-derived  $R_s$  site data.



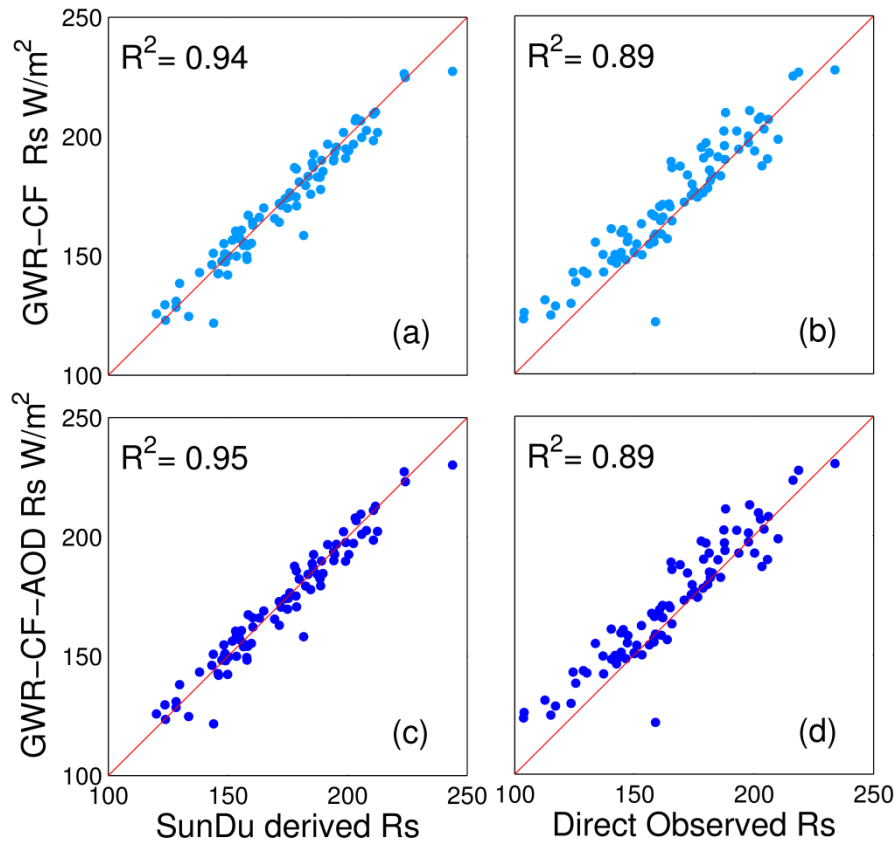
432 **Figure 5.** Seasonal and annual variations in  $R_s$  at two sites: Chang Chun (a and c,  
 433 43.87°N and 125.33°E) and Bei Hai (b and d, 23.50°N, 99.72°E). SunDu  $R_s$  is the  
 434 SunDu-derived  $R_s$  data, and GWR-CF  $R_s$  is  $R_s$  produced by the GWR method  
 435

436 incorporating only the cloud fraction. GWR-CF-AOD is  $R_s$  produced by the GWR  
437 method incorporating cloud fraction and AOD. The multiyear mean of AOD from  
438 Changchun and BeiHai are 0.49 and 0.70, respectively.

439 We also analyse the performances of fusion methods for different seasons at all  
440 validation sites, as shown in **Table 4**. At seasonal scales, both the GWR-CF and GWR-  
441 CF-AOD methods have high  $R^2$  values ranging from 0.94 to 0.96, compared with direct  
442  $R_s$  measurement or SunDu-derived  $R_s$ . GWR-CF and GWR-CF-AOD show slight  
443 differences, indicating that both fusion methods produce consistent  $R_s$  seasonal  
444 variation patterns, which might be because the impacts of AOD have already been  
445 included in the SunDu-derived  $R_s$  site data at seasonal time scales. Comparatively, the  
446 GWR methods perform best in autumn, with RMSEs ranging from 9.23W/m<sup>2</sup> to 9.56  
447 W/m<sup>2</sup> followed by winter, spring and summer. Both the GWR-CF and GWR-CF-AOD  
448 methods produce similar annual variations in  $R_s$  from 2000 to 2016, with  $R^2$  values  
449 ranging from 0.57 to 0.58 (**Table 4**). The statistics indicate that the GWR can produce  
450 reasonable seasonal and annual variations in  $R_s$ .

### 451 **3.3 Multiyear mean and long-term variability in $R_s$**

452 **Figure 6** shows the performance of GWR-CF and GWR-CF-AOD on simulating  
453 the multiyear mean  $R_s$  by using 97 direct  $R_s$  observation sites and independent SunDu-  
454 derived  $R_s$  sites. Based on direct  $R_s$  measurements, both GWR-based methods show  
455 good performances with high  $R^2$  (0.89~0.95) and low RMSE (11.03~11.11 W/m<sup>2</sup>), and  
456 few differences are found for the GWR merging results, whether or not AOD is taken  
457 as input data (**Table 4**).

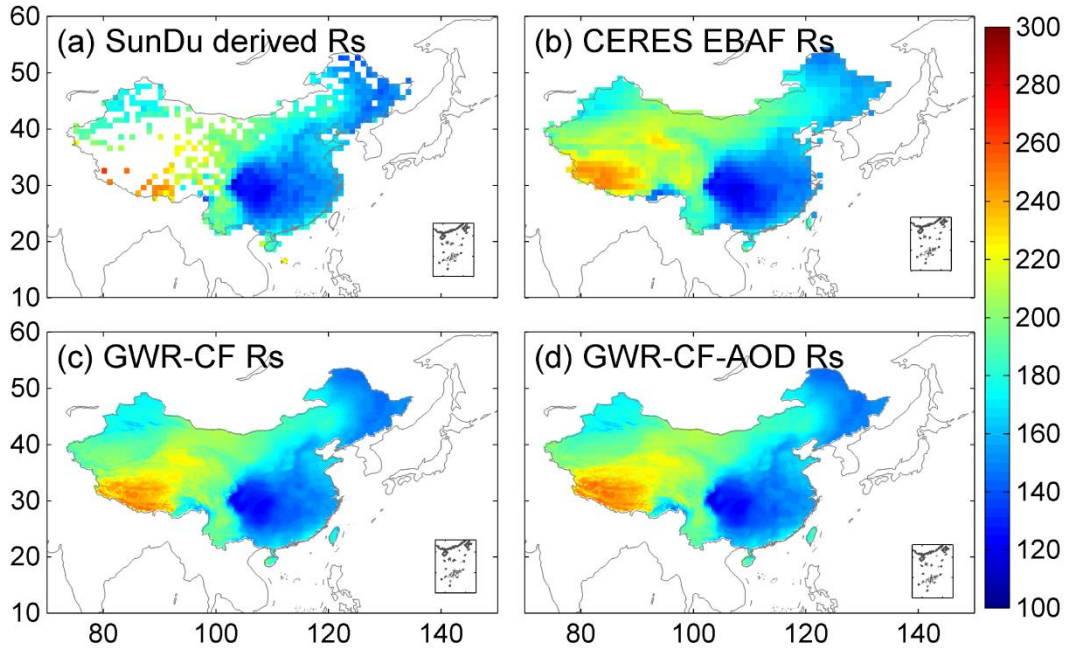


458

459 **Figure 6.** Comparison of multiyear mean surface solar radiation ( $R_s$ ) derived from the  
 460 GWR method. Subplots (a, c) represent validation results using SunDu-derived  $R_s$  data  
 461 as a reference, while that of subplots (b, d) use direct observed  $R_s$  data.

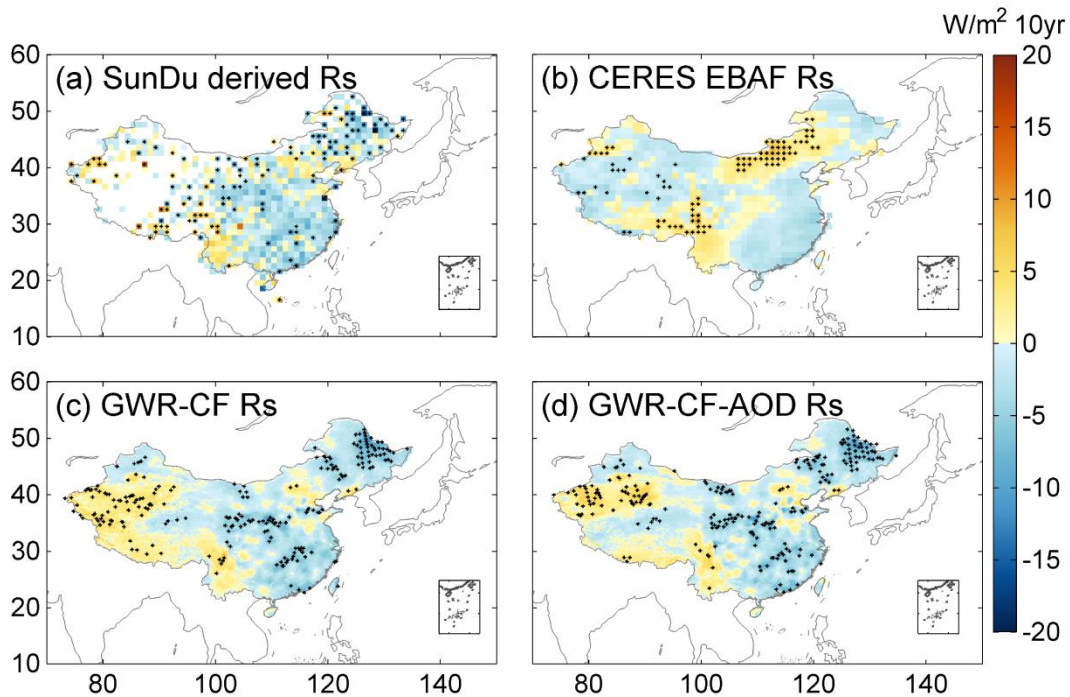
462 The spatial distributions of the multiyear means of  $R_s$  from 2000 to 2017 are shown  
 463 in **Figure 7**. The SunDu sites show that  $R_s$  is high in northwest China, ranging from 180  
 464 to 300  $W/m^2$ , and low in eastern China, ranging from 120 to 180  $W/m^2$ . Both the GWR-  
 465 CF and GWR-CF-AOD methods show consistent  $R_s$  spatial patterns with SunDu-  
 466 derived  $R_s$  observations and CERES EBAFs, indicating that the relationship between  
 467  $R_s$  and impact factors is not linearly stable and is closely related to spatial position. The  
 468 spatial distribution of the  $R_s$  trend derived from the GWR method is also consistent with  
 469 the SunDu-derived  $R_s$  trend, especially in western China (**Fig. 8**).





470

471 **Figure 7.** Spatial distribution of multiyear mean monthly surface solar radiation ( $R_s$ )  
 472 from 2000 to 2017. The first line (a, b) shows the observed multiyear mean monthly  $R_s$   
 473 from SunDu and CERES EBAF; the multiyear mean monthly  $R_s$  derived from the GWR  
 474 method are shown in the second line (c, d), respectively.



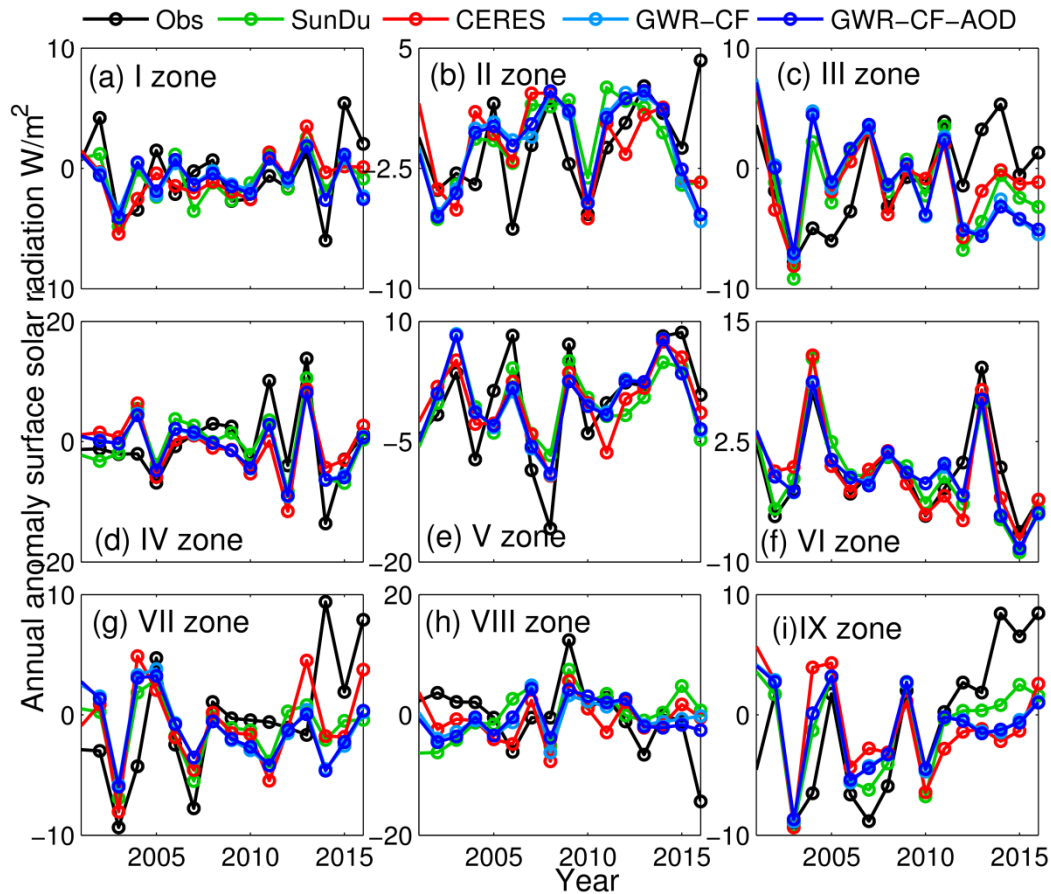
475

476 **Figure 8.** Spatial distributions of monthly anomaly trends of surface solar radiation ( $R_s$ )  
 477 from 2000 to 2017. The first line (a, b) shows the SunDu-derived  $R_s$  and CERES EBAF

478  $R_s$ ; the  $R_s$ -derived GWR fusion methods are shown in the second line (c, d). Subplots  
479 (c) incorporate only CF, and subplots (d) incorporate CF and AOD. The black dots on  
480 the maps represent significant trends ( $P < 0.05$ ).

481 Based on the classified subregions using 97 direct  $R_s$  observations in **Figure 1**, the  
482 regional means of  $R_s$  annual anomaly variation from 2000 to 2016 are shown in **Figure**  
483 **9**. Compared with observations, both the GWR-CF and GWR-CF-AOD methods  
484 produce consistent long-term  $R_s$  trends with SunDu-derived  $R_s$  and CERES EBAF  $R_s$   
485 (**Figures 2, 3 and 9**), indicating that the GWR-CF and GWR-CF-AOD methods can  
486 produce reasonable annual  $R_s$  variations over China.

487 In zones I and II, located in northern arid/semiarid regions, the annual anomaly  $R_s$   
488 variation shows small fluctuations ranging from -10 to 10  $W/m^2$ . In contrast, zones IV,  
489 V, VIII and IX covering the Sichuan Basin, Yunnan-Guizhu Plateau, Qinghai-Tibet  
490 Plateau and North China Plain show large  $R_s$  variation trends. Li et al. (2018) found a  
491 sharply increasing  $R_s$  trend over East China, especially in the North China Plain, which  
492 is due to controlling air pollution and reducing aerosol loading. However, our results  
493 indicate that the increased surface solar radiation in North China is not confirmed by  
494 satellite retrieval (CERES) and SunDu-derived  $R_s$ .



495

496 **Figure 9.** The regional mean of the annual anomaly of the surface solar radiation ( $R_s$ )  
 497 for different subregions. Nine subregions (I to IX) over China are shown in Figure 1.  
 498 Direct  $R_s$  observations, SunDu-derived  $R_s$ , and CERES EBAF are shown as black lines,  
 499 green lines and red lines, respectively. Light and dark blue represent the  $R_s$  variation  
 500 derived from the GWR-CF and the GWR-CF-AOD methods.

501

## 502 4. Discussion

### 503 4.1 Impact factors of $R_s$

504 In this study, we merged more than 2400 sunshine duration-derived  $R_s$  site data  
 505 with MODIS CF and AOD data to generate high spatial resolution ( $0.1^\circ$ )  $R_s$  over China  
 506 from 2000 to 2017. The results show that the GWR method incorporated with CF and

507 AOD (GWR-CF-AOD) performs best, indicating the non-neglected role of clouds and  
508 aerosols in regulating the variation in  $R_s$  over China.

509 Clouds and aerosols impact the solar radiation reaching the surface by radiative  
510 absorption and scattering (Tang et al., 2017). Recent  $R_s$  trend studies over Europe  
511 suggest that CF may play a key role in the positive trend of  $R_s$  since the 1990s (Pfeifroth  
512 et al., 2018a). In terms of input data, our results also indicate that the cloud fraction  
513 might be a major factor affecting  $R_s$ , which is consistent with our previous studies (Feng  
514 and Wang, 2019).

515 Changes in aerosol loading have also been reported to be an important impact  
516 factor (Che et al., 2005; Li et al., 2018; Liang and Xia, 2005; Qian et al., 2015; Xia,  
517 2010; Zhou et al., 2019b). The atmospheric visibility data show that the slope of the  
518 linear variation in surface solar radiation with respect to atmospheric visibility is  
519 distinctly different at different stations (Yang et al., 2017), implying that the relationship  
520 between  $R_s$  and aerosols varies with location.

#### 521 **4.2 Performances of the fusion methods**

522 The good overall performances of the GWR model have been reported in many  
523 previous studies, including geography (Chao et al., 2018; Georganos et al., 2017),  
524 economics (Ma and Gopal, 2018), meteorology (Li and Meng, 2017; Zhou et al., 2019a),  
525 and epidemiology (Tsai and Teng, 2016). Chao et al. (2018) used the GWR method to  
526 merge satellite precipitation and gauge observations to correct biases in satellite  
527 precipitation data and downscale satellite precipitation to a finer spatial resolution at  
528 the same time. Zhou et al. (2019a) used GWR to analyse haze pollution over China and  
529 found that the GWR estimate was better than the OLS estimate, with an improvement  
530 in correlation coefficient from 0.20 to 0.75.

531 Compared with other traditional interpolation methods, such as optimal

532 interpolation (OI), GWR can theoretically integrate geographical location and  $R_s$  impact  
533 factors for spatial  $R_s$  estimations and reflect the non-stationary spatial relationship  
534 between  $R_s$  and its impact factors. The thin plate spline method can include CF and  
535 AOD as covariates to simulate the approximately linear dependence of these impact  
536 factors on  $R_s$ , but this linear function cannot fully describe the relationship among CF,  
537 AOD and  $R_s$  (Hong et al., 2005).

538 Comparison results from (Wang et al., 2017) also indicate that the GWR method  
539 is better than the multiple linear regression method and spline interpolation method for  
540 near surface air temperature. By using spatial interpolation method, CERES EBAF  $R_s$   
541 can also be downscaled to 1km or 30m. These interpolated CERES  $R_s$  data cannot  
542 represent the detailed  $R_s$  distributions at spatial resolution of 1km or 30m due to the  
543 variability of  $R_s$  within a 1 degree box. Without additional high spatial resolution data,  
544 interpolated cannot capture more detail variability of  $R_s$ .

545

## 546 **5. Data availability**

547 The merged  $R_s$  product by GWR methods with cloud fraction and AOD data as  
548 input in this study are available at <https://doi.pangaea.de/10.1594/PANGAEA.921847>  
549 (Feng and Wang, 2020).

## 550 **6. Conclusions**

551 Accurate estimation of  $R_s$  variability is crucially important for regional energy  
552 budget, water cycle and climate change studies. Recent studies have shown that SunDu-  
553 derived  $R_s$  data can provide reliable long-term  $R_s$  series. In this study, we merged  
554 SunDu-derived  $R_s$  data with satellite-derived cloud fraction (CF) and aerosol optical

555 depth (AOD) data to generate high spatial resolution ( $0.1^\circ$ )  $R_s$  over China from 2000 to  
556 2017 (Feng and Wang, 2020). The GWR and OLS merging methods were also  
557 compared.

558 Our results show that the spatial resolutions of all fusion results are improved to  
559  $0.1^\circ$  by incorporating MODIS cloud fraction data. The GWR shows better performance  
560 than OLS, with increases in  $R^2$  by 9.21%~12.81% and RMSEs reduced by  
561 49.56%~54.68%, indicating that  $R_s$  has complex characteristics of spatial variability  
562 over China, which has also indicated the necessity of the high spatial resolution of  $R_s$   
563 data. As clouds and aerosols play vital roles in the variability in  $R_s$ , apparent  
564 improvements in the results of SunDu-derived  $R_s$  data merging are found if both cloud  
565 fraction and AOD are incorporated. Based on the merging results incorporating only  
566 cloud fraction, cloud fraction is suggested to be the major factor impacting  $R_s$ , which  
567 explained approximately 86%~97% of  $R_s$  variability. Generally, SunDu-derived  $R_s$  data  
568 merging results derived from GWR show more consistent multiyear mean  $R_s$  and long-  
569 term  $R_s$  trends compared with those from OLS. Our results show that the improvement  
570 in  $R_s$  variability estimation is closely related to  $R_s$  impact factors and  $R_s$  spatial  
571 heterogeneity. The merged  $R_s$  products derived from GWR-CF-AOD can be  
572 downloaded at <https://doi.pangaea.de/10.1594/PANGAEA.921847>.

## 573 **Acknowledgements**

574 This study was funded by the National Key Research & Development Program of  
575 China (2017YFA06036001), the National Natural Science Foundation of China  
576 (41525018), the Fundamental Research Funds for the Central Universities  
577 (#BLX201907), and the State Key Laboratory of Earth Surface Processes and Resource  
578 Ecology (U2020-KF-02). We would like to thank Chengyang Xu, Yuna Mao, Jizeng Du,

579 Runze Li, Qian Ma, Guocan Wu, and Chunlue Zhou for their insightful comments. We  
580 are grateful to Amelie Driemel for her help of uploading the data in PANGAEA. The  
581 cloud data can be downloaded from  
582 [https://neo.sci.gsfc.nasa.gov/view.php?datasetId=MODAL2\\_M\\_CLD\\_FR](https://neo.sci.gsfc.nasa.gov/view.php?datasetId=MODAL2_M_CLD_FR). The  
583 CERES SYN data can be downloaded from <https://ceres.larc.nasa.gov/data/>.  
584  
585

## References

586

587 Ali, K., Partridge, M. D., and Olfert, M. R.: Can Geographically Weighted Regressions  
588 Improve Regional Analysis and Policy Making?, *Int. Reg. Sci. Rev.*, 30, 300-329,  
589 2007.

590 Brunsdon, C., Fotheringham, A. S., and Charlton, M. E.: Geographically Weighted  
591 Regression : A Method for Exploring Spatial Nonstationarity, *geographical  
592 analysis*, 28, 281-298, 2010.

593 Brunsdon, C., Fotheringham, S., and Charlton, M.: Geographically Weighted  
594 Regression. 1998.

595 Camargo, L. R. and Dorner, W.: Integrating satellite imagery derived data and GIS-  
596 based solar radiation algorithms to map solar radiation in high temporal and spatial  
597 resolutions for the province of Salta, Argentina, *SPIE Remote Sensing*, 100050E,  
598 2016.

599 Chao, L., Zhang, K., Li, Z., Zhu, Y., Wang, J., and Yu, Z.: Geographically weighted  
600 regression based methods for merging satellite and gauge precipitation, *J. Hydrol.*,  
601 558, 275-289, 2018.

602 Che, H. Z., Shi, G. Y., Zhang, X. Y., Arimoto, R., Zhao, J. Q., Xu, L., Wang, B., and  
603 Chen, Z. H.: Analysis of 40 years of solar radiation data from China, 1961–2000,  
604 *Geophys. Res. Lett.*, 1029, 2341-2352, 2005.

605 Collins, W. D., Rasch, P. J., Eaton, B. E., Khattatov, B. V., Lamarque, J. F., and Zender,  
606 C. S.: Simulating aerosols using a chemical transport model with assimilation of  
607 satellite aerosol retrievals: Methodology for INDOEX, *J. Geophys. Res.*, 106,  
608 7313-7336, 2001.

609 Cornejo-Bueno, L., Casanova-Mateo, C., Sanz-Justo, J., and Salcedo-Sanz, S.: Machine  
610 learning regressors for solar radiation estimation from satellite data, *Sol. Energy*,



611 183, 768-775, 2019.

612 Dai, A., Karl, T. R., Sun, B., and Trenberth, K. E.: Recent Trends in Cloudiness over  
613 the United States: A Tale of Monitoring Inadequacies, *Bull. Am. Meteorol. Soc.*,  
614 87, 597-606, 2006.

615 Doelling, D. R., Loeb, N. G., Keyes, D. F., Nordeen, M. L., Morstad, D., Nguyen, C.,  
616 Wielicki, B. A., Young, D. F., and Sun, M.: Geostationary Enhanced Temporal  
617 Interpolation for CERES Flux Products, *J. Atmos. Ocean Technol.*, 30, 1072-1090,  
618 2013.

619 Evan, A. T., Heidinger, A. K., and Vimont, D. J.: Arguments against a physical long  
620 term trend in global ISCCP cloud amounts, *Geophys. Res. Lett.*, 34, 290-303, 2007.

621 Feng, F. and Wang, K.C.: Determining Factors of Monthly to Decadal Variability in  
622 Surface Solar Radiation in China: Evidences From Current Reanalyses, *J.*  
623 *Geophys. Res. Atmos.*, 124, 9161-9182, 2019.

624 Feng, F. and Wang, K. C.: Merging Satellite Retrievals and Reanalyses to Produce  
625 Global Long-Term and Consistent Surface Incident Solar Radiation Datasets,  
626 *Remote Sens.*, 10, 115, 2018.

627 Feng, F. and Wang, K. C.: Monthly surface solar radiation data over China (2000-2017)  
628 by merging satellite cloud and aerosol data with ground-based sunshine duration  
629 data. PANGAEA, <https://doi.pangaea.de/10.1594/PANGAEA.921847>, 2020.

630 Feng, Y., Chen, D., and Zhao, X.: Estimated long-term variability of direct and diffuse  
631 solar radiation in North China during 1959–2016, *Theor.Appl. Climatol.*, 137,  
632 153-163, 2019.

633 Fotheringham, A. S., Charlton, M., and Brunson, C.: The geography of parameter  
634 space: an investigation of spatial non-stationarity, *Int. J. Geogr. Inf. Syst.*, 10, 605-  
635 627, 1996.

636 Gao, X., Asami, Y., and Chung, C.-J. F.: An empirical evaluation of spatial regression  
637 models, *Comput. Geosci.*, 32, 1040-1051, 2006.

638 Georganos, S., Abdi, A. M., Tenenbaum, D. E., and Kalogirou, S.: Examining the  
639 NDVI-rainfall relationship in the semi-arid Sahel using geographically weighted  
640 regression, *J. Arid Environ.*, 146, 64-74, 2017.

641 Hakuba, M. Z., Folini, D., Schaepman-Strub, G., and Wild, M.: Solar absorption over  
642 Europe from collocated surface and satellite observations, *J. Geophys. Res.*, 119,  
643 3420-3437, 2014.

644 He, Y., Wang, K., Zhou, C., and Wild, M.: A Revisit of Global Dimming and  
645 Brightening Based on the Sunshine Duration, *Geophys. Res. Lett.*, 45(9), 4281-  
646 4289, 2018.

647 He, Y. and Wang, K. C.: Variability in direct and diffuse solar radiation across China  
648 from 1958 to 2017, *Geophys. Res. Lett.*, 47, 2020.

649 Hong, Y., Nix, H. A., Hutchinson, M. F., and Booth, T. H.: Spatial interpolation of  
650 monthly mean climate data for China, *Int. J. Climatol.*, 25, 1369-1379, 2005.

651 Hongrong, S., Weiwei, L., Xuehua, F., Jinqiang, Z., Bo, H., Letu, H., Huazhe, S., Xinlei,  
652 H., Zijue, S., and Yingjie, Z.: First assessment of surface solar irradiance derived  
653 from Himawari-8 across China, *Sol. Energy*, 174, 164-170, 2018.

654 Hou, N., Zhang, X., Zhang, W., Xu, J., Feng, C., Yang, S., Jia, K., Yao, Y., Cheng, J.,  
655 and Jiang, B.: A New Long-Term Downward Surface Solar Radiation Dataset over  
656 China from 1958 to 2015, *Sensors (Basel)*, 20, 2020.

657 Huang, G., Li, Z., Li, X., Liang, S., Yang, K., Wang, D., and Zhang, Y.: Estimating  
658 surface solar irradiance from satellites: Past, present, and future perspectives,  
659 *Remote Sens. Environ.*, 233, 111371, 2019.

660 Jia, B., Xie, Z., Dai, A., Shi, C., and Chen, F.: Evaluation of satellite and reanalysis

661 products of downward surface solar radiation over East Asia: Spatial and seasonal  
662 variations, *J. Geophys. Res. Atmos.*, 118, 3431-3446, 2013.

663 Jin, H.-a., Li, A.-n., Bian, J.-h., Zhang, Z.-j., Huang, C.-q., and Li, M.-x.: Validation of  
664 global land surface satellite (GLASS) downward shortwave radiation product in  
665 the rugged surface, *J Mt. Sci.*, 10, 812-823, 2013.

666 Jin, Z., Yezheng, W., and Gang, Y.: General formula for estimation of monthly average  
667 daily global solar radiation in China, *Energy Convers.Manag.*, 46, 257-268, 2005.

668 Journée, M. and Bertrand, C.: Improving the spatio-temporal distribution of surface  
669 solar radiation data by merging ground and satellite measurements, *Remote Sens.*  
670 *Environ.*, 114, 2692-2704, 2010.

671 Journée, M., Müller, R., and Bertrand, C.: Solar resource assessment in the Benelux by  
672 merging Meteosat-derived climate data and ground measurements, *Sol. Energy*, 86,  
673 3561-3574, 2012.

674 Karlsson, K.-G., Anttila, K., Trentmann, J., Stengel, M., Meirink, J. F., Devasthale, A.,  
675 Hanschmann, T., Kothe, S., Jääskeläinen, E., and Sedlar, J.: CLARA-A2: the  
676 second edition of the CM SAF cloud and radiation data record from 34 years of  
677 global AVHRR data, *Atmos. Chem. Phys.*, 17, 1-41, 2017.

678 Kato, S., Rose, F. G., Rutan, D. A., Thorsen, T. J., Loeb, N. G., Doelling, D. R., Huang,  
679 X., Smith, W. L., Su, W., and Ham, S.-H.: Surface Irradiances of Edition 4.0  
680 Clouds and the Earth's Radiant Energy System (CERES) Energy Balanced and  
681 Filled (EBAF) Data Product, *J. Clim.*, 31, 4501-4527, 2018.

682 Leckner, B. G.: The spectral distribution of solar radiation at the earth's surface—  
683 elements of a model, *Sol. Energy*, 20, 143-150, 1978.

684 LeSage, J. P.: *A Family of Geographically Weighted Regression Models*. 2004.

685 Letu, H., Yang, K., Nakajima, T. Y., Ishimoto, H., Nagao, T. M., Riedi, J., Baran, A. J.,

686 Ma, R., Wang, T., Shang, H., Khatri, P., Chen, L., Shi, C., and Shi, J.: High-  
687 resolution retrieval of cloud microphysical properties and surface solar radiation  
688 using Himawari-8/AHI next-generation geostationary satellite, *Remote Sens.*  
689 *Environ.*, 239, 111583, 2020.

690 Li, J., Jiang, Y. W., Xia, X. G., and Hu, Y. Y.: Increase of surface solar irradiance across  
691 East China related to changes in aerosol properties during the past decade,  
692 *Environ.Res. Lett.*, 13, 034006, 2018.

693 Li, T. and Meng, Q.: Forest dynamics to precipitation and temperature in the Gulf of  
694 Mexico coastal region, *Int. J. Biometeorol.*, 61, 869-879, 2017.

695 Liang, F. and Xia, X. A.: Long-term trends in solar radiation and the associated climatic  
696 factors over China for 1961-2000, *Annales Geophysicae*, 23, 2425-2432, 2005.

697 Loghmari, I., Timoumi, Y., and Messadi, A.: Performance comparison of two global  
698 solar radiation models for spatial interpolation purposes, *Renew.Sust. Energ. Rev.*,  
699 82, 837-844, 2018.

700 Lorenzo, A. T., Morzfeld, M., Holmgren, W. F., and Cronin, A. D.: Optimal  
701 interpolation of satellite and ground data for irradiance nowcasting at city scales,  
702 *Sol. Energy*, 144, 466-474, 2017.

703 Lu, W., Mo, Y., and Wang, D.: Characteristics investigation for pyranometers, *Acta*  
704 *Energi. Sin.*, 23, 313–316, 2002.

705 Lu, W. H. and Bian, Z. Q.: Station experiment and preliminary data analysis of high-  
706 precision solar radiation measurement system, *Meteorol. Hydrol. Mar. Instrum.*, 3,  
707 1-5, 2012.

708 Luo, Y., Lu, D., Zhou, X., Li, W., and He, Q.: Characteristics of the spatial distribution  
709 and yearly variation of aerosol optical depth over China in last 30 years, *J.*  
710 *Geophys. Res.*, 106, 14501-14513, 2001.

711 Ma, Q., Wang, K. C., and Wild, M.: Impact of geolocations of validation data on the  
712 evaluation of surface incident shortwave radiation from Earth System Models, *J.*  
713 *Geophys. Res. Atmos.*, 120, 6825-6844, 2015.

714 Ma, Y. and Gopal, S.: Geographically Weighted Regression Models in Estimating  
715 Median Home Prices in Towns of Massachusetts Based on an Urban Sustainability  
716 Framework, *Sustainability*, 10, 1026, 2018.

717 Manara, V., Beltrano, M. C., Brunetti, M., Maugeri, M., Sanchez-Lorenzo, A., Simolo,  
718 C., and Sorrenti, S.: Sunshine duration variability and trends in Italy from  
719 homogenized instrumental time series (1936–2013), *J. Geophys. Res. Atmos.*, 120,  
720 3622-3641, 2015.

721 Manara, V., Brunetti, M., Maugeri, M., Sanchez-Lorenzo, A., and Wild, M.: Sunshine  
722 duration and global radiation trends in Italy (1959–2013): To what extent do they  
723 agree?, *J. Geophys. Res.*, 122, 4312-4331, 2017.

724 Mo, Y. Q., Yang, Y., Liang, H. L., and Wang, D.: Investigation report on technology of  
725 status and development of meteorological radiation observation in China, *Chinese*  
726 *J. Sci. Instrum.*, 29, 518–522, 2008.

727 Montero-Martín, J., Antón, M., Vaquero-Martínez, J., and Sanchez-Lorenzo, A.:  
728 Comparison of long-term solar radiation trends from CM SAF satellite products  
729 with ground-based data at the Iberian Peninsula for the period 1985–2015, *Atmos.*  
730 *Res.*, 236, 104839, 2020.

731 Myers, D. R.: Solar radiation modeling and measurements for renewable energy  
732 applications: data and model quality, *Energy*, 30, 1517-1531, 2005.

733 Pfeifroth, U., Bojanowski, J. S., Clerbaux, N., Manara, V., Sanchez-Lorenzo, A.,  
734 Trentmann, J., Walawender, J. P., Hollmann, R., and Jakub, W. P.: Satellite-based  
735 trends of solar radiation and cloud parameters in Europe, *Adv. Sci. Res.*, 15, 31-

736 37, 2018a.

737 Pfeifroth, U., Sanchez-Lorenzo, A., Manara, V., Trentmann, J., and Hollmann, R.:  
738 Trends and Variability of Surface Solar Radiation in Europe Based On Surface  
739 and Satellite-Based Data Records, *J. Geophys. Res. Atmos.*, 123, 1735–1754, 2018b.

740 Platnick, S., Ackerman, S., King, M., Wind, G., Meyer, K., Menzel, W., Holz, R., Baum,  
741 B., and Yang, P.: MODIS atmosphere L2 cloud product (06\_L2), NASA MODIS  
742 Adaptive Processing System, Goddard Space Flight Center, 1, 1, 2017.

743 Qian, Y., Kaiser, D. P., Leung, L. R., and Xu, M.: More frequent cloud-free sky and  
744 less surface solar radiation in China from 1955 to 2000, *Geophys. Res. Lett.*, 33,  
745 311-330, 2015.

746 Rahman, M. and Zhang, W.: Review on estimation methods of the Earth's surface  
747 energy balance components from ground and satellite measurements, *J Earth Syst.*  
748 *Sci.*, 128, 2019.

749 Ruiz-Arias, J. A., Quesada-Ruiz, S., Fernández, E. F., and Gueymard, C. A.: Optimal  
750 combination of gridded and ground-observed solar radiation data for regional solar  
751 resource assessment, *Sol. Energy*, 112, 411-424, 2015.

752 Rutan, D. A., Kato, S., Doelling, D. R., Rose, F. G., Nguyen, L. T., Caldwell, T. E., and  
753 Loeb, N. G.: CERES Synoptic Product: Methodology and Validation of Surface  
754 Radiant Flux, *J. Atmos. Ocean Technol.*, 32, 1121-1143, 2015.

755 Sanchezlorenzo, A., Azorinmolina, C., Wild, M., Vicenteserrano, S. M., Lópezmoreno,  
756 J. I., and Corellcustardoy, D.: Feasibility of sunshine duration records to detect  
757 changes in atmospheric turbidity: A case study in Valencia (Spain), *AIP Conf.*  
758 *Proc.*, 736-739, 2013.

759 Sanchezlorenzo, A., Calbó, J., Brunetti, M., and Deser, C.: Dimming/brightening over  
760 the Iberian Peninsula: Trends in sunshine duration and cloud cover and their

761 relations with atmospheric circulation, *J. Geophys. Res. Atmos.*, 114, 114,  
762 D100D109, doi:110.1029/2008JD011394., 2009.

763 Sanchezromero, A., Sanchezlorenzo, A., Calbó, J., González, J. A., and Azorin-Molina,  
764 C.: The signal of aerosol-induced changes in sunshine duration records: A review  
765 of the evidence, *J. Geophys. Res. Atmos.*, 119, 4657–4467, 2014.

766 Schwarz, M., Folini, D., Yang, S., Allan, R. P., and Wild, M.: Changes in atmospheric  
767 shortwave absorption as important driver of dimming and brightening, *Nat.*  
768 *Geosci.*, 13, 110-115, 2020.

769 Sheehan, K. R., Strager, M. P., and Welsh, S. A.: Advantages of Geographically  
770 Weighted Regression for Modeling Benthic Substrate in Two Greater Yellowstone  
771 Ecosystem Streams, *Environ. Monit. Assess.*, 18, 209-219, 2012.

772 Shi, G.-Y., Hayasaka, T., Ohmura, A., Chen, Z.-H., Wang, B., Zhao, J.-Q., Che, H.-Z.,  
773 and Xu, L.: Data Quality Assessment and the Long-Term Trend of Ground Solar  
774 Radiation in China, *J. Appl. Meteorol. Climatol.*, 47, 1006-1016, 2008.

775 Stengel, M., Stapelberg, S., Sus, O., Finkensieper, S., Würzler, B., Philipp, D.,  
776 Hollmann, R., Poulsen, C., Christensen, M., and McGarragh, G.: Cloud\_cci  
777 Advanced Very High Resolution Radiometer post meridiem (AVHRR-PM) dataset  
778 version 3: 35-year climatology of global cloud and radiation properties, *Earth Syst.*  
779 *Sci. Data*, 12, 41-60, 2020.

780 Tang, W., Yang, K., Qin, J., Li, X., and Niu, X.: A 16-year dataset (2000–2015) of high-  
781 resolution (3 h, 10 km) global surface solar radiation, *Earth Syst. Sci. Data*, 11,  
782 1905-1915, 2019.

783 Tang, W., Yang, K., Qin, J., Niu, X., Lin, C., and Jing, X.: A revisit to decadal change  
784 of aerosol optical depth and its impact on global radiation over China, *Atmospheric*  
785 *Environment*, 150, 106e115, 2017.

786 Tang, W. J., Yang, K., Qin, J., Cheng, C. C. K., and He, J.: Solar radiation trend across  
787 China in recent decades: a revisit with quality-controlled data, *Atmos. Chem. Phys.*,  
788 11, 393-406, 2011.

789 Tsai, P. and Teng, H.: Role of *Aedes aegypti* (Linnaeus) and *Aedes albopictus* (Skuse)  
790 in local dengue epidemics in Taiwan, *BMC Infectious Diseases*, 16, 662, 2016.

791 Wang, K. C.: Measurement biases explain discrepancies between the observed and  
792 simulated decadal variability of surface incident solar radiation, *Sci. Rep.*, 4, 6144,  
793 2014.

794 Wang, K. C. and Dickinson, R. E.: Contribution of solar radiation to decadal  
795 temperature variability over land, *Proc. Natl. Acad. Sci. U.S.A.*, 110, 14877, 2013.

796 Wang, K. C., Ye, H., Chen, F., Xiong, Y., and Wang, C.: Urbanization Effect on the  
797 Diurnal Temperature Range: Different Roles under Solar Dimming and  
798 Brightening\*, *J. Clim.*, 25, 1022-1027, 2012a.

799 Wang, K. C., Ma, Q., Li, Z., and Wang, J.: Decadal variability of surface incident solar  
800 radiation over China: Observations, satellite retrievals, and reanalyses, *J. Geophys.*  
801 *Res. Atmos.*, 120, 6500-6514, 2015.

802 Wang, M., He, G., Zhang, Z., Wang, G., Zhang, Z., Cao, X., Wu, Z., and Liu, X.:  
803 Comparison of Spatial Interpolation and Regression Analysis Models for an  
804 Estimation of Monthly Near Surface Air Temperature in China, *Remote Sens.*, 9,  
805 1278, 2017.

806 Wang, Y., Yang, Y., Zhao, N., Liu, C., and Wang, Q.: The magnitude of the effect of air  
807 pollution on sunshine hours in China, *J. Geophys. Res. Atmos.*, 117, 116-116, 2012b.

808 Wei, Y., Zhang, X., Hou, N., Zhang, W., Jia, K., and Yao, Y.: Estimation of surface  
809 downward shortwave radiation over China from AVHRR data based on four  
810 machine learning methods, *Sol. Energy*, 177, 32-46, 2019.



811 Wild, M.: Decadal changes in radiative fluxes at land and ocean surfaces and their  
812 relevance for global warming, *Wiley Interdisciplinary Reviews Climate Change*,  
813 7, 91-107, 2016.

814 Wild, M.: Global dimming and brightening: A review, *J. Geophys. Res. Atmos.*, 114,  
815 D00D16, 2009.

816 Wild, M.: Towards Global Estimates of the Surface Energy Budget, *Curr. Clim. Change*  
817 *Rep.*, 2017. 1-11, 2017.

818 Xia, X.: Spatiotemporal changes in sunshine duration and cloud amount as well as their  
819 relationship in China during 1954–2005, *J. Geophys. Res. Atmos.*, 115, 86, 2010.

820 Yang, H., Li, Z., Li, M., and Yang, D.: Inconsistency in Chinese solar radiation data  
821 caused by instrument replacement: Quantification based on pan evaporation  
822 observations, *J. Geophys. Res.*, 120, 3191-3198, 2015.

823 Yang, K., Koike, T., and Ye, B.: Improving estimation of hourly, daily, and monthly  
824 solar radiation by importing global data sets, *Agric. For. Meteorol.*, 137, 43-55,  
825 2006.

826 Yang, L., Cao, Q., Yu, Y., and Liu, Y.: Comparison of daily diffuse radiation models in  
827 regions of China without solar radiation measurement, *energy*, 191, 2020.

828 Yang, S., Wang, X. L., and Wild, M.: Homogenization and Trend Analysis of the 1958–  
829 2016 In Situ Surface Solar Radiation Records in China, *J. Clim.*, 31, 4529-4541,  
830 2018.

831 Yang, X., Zhao, C., Zhou, L., Wang, Y., and Liu, X.: Distinct impact of different types  
832 of aerosols on surface solar radiation in China, *J. Geophys. Res. Atmos.*, 121, 2017.

833 Yang, Y., Ding, L., and Wang, D.: Experiments and analysis of pyranometer on  
834 nighttime zero offset, *Meteorol. Mon.*, 36, 100-103, 2010.

835 Yeom, J. M., Park, S., Chae, T., Kim, J. Y., and Lee, C. S.: Spatial Assessment of Solar

836 Radiation by Machine Learning and Deep Neural Network Models Using Data  
837 Provided by the COMS MI Geostationary Satellite: A Case Study in South Korea,  
838 Sensors (Basel), 19, 2019.

839 Zell, E., Gasim, S., Wilcox, S., Katamoura, S., Stoffel, T., Shibli, H., Engel-Cox, J., and  
840 Al Subie, M.: Assessment of solar radiation resources in Saudi Arabia, Sol. Energy,  
841 119, 422-438, 2015.

842 Zhang, X., Liang, S., Wang, G., Yao, Y., Jiang, B., and Cheng, J.: Evaluation of the  
843 reanalysis surface incident shortwave radiation products from NCEP, ECMWF,  
844 GSFC, and JMA using satellite and surface observations, Remote Sens., 8, 225-  
845 249, 2016.

846 Zhang, X., Liang, S., Wild, M., and Jiang, B.: Analysis of surface incident shortwave  
847 radiation from four satellite products, Remote Sens. Environ., 165, 186-202, 2015.

848 Zhang, Y., Rossow, W. B., Lacis, A. A., Oinas, V., and Mishchenko, M. I.: Calculation  
849 of radiative fluxes from the surface to top of atmosphere based on ISCCP and other  
850 global data sets: Refinements of the radiative transfer model and the input data, J.  
851 Geophys. Res. Atmos., 109, 2004.

852 Zhao, L., Lee, X., and Liu, S.: Correcting surface solar radiation of two data  
853 assimilation systems against FLUXNET observations in North America, J.  
854 Geophys. Res. Atmos., 118, 9552-9564, 2013.

855 Zhou, Q., Wang, C., and Fang, S.: Application of geographically weighted regression  
856 (GWR) in the analysis of the cause of haze pollution in China, Atmospheric  
857 Pollut. Res., 10, 835-846, 2019a.

858 Zhou, Z., Lin, A., Wang, L., Qin, W., zhong, Y., and He, L.: Trends in downward surface  
859 shortwave radiation from multi-source data over China during 1984–2015, Int. J.  
860 Climatol., 40, 1-19, 2019b.

861 Zou, L., Wang, L., Lin, A., Zhu, H., Peng, Y., and Zhao, Z.: Estimation of global solar  
862 radiation using an artificial neural network based on an interpolation technique in  
863 southeast China, *J. Atmos. Sol. Terr. Phys.*, 146, 110-122, 2016.

864

865